Chaos, Solitons and Fractals 165 (2022) 112776

Contents lists available at ScienceDirect

Chaos, Solitons and Fractals

journal homepage: www.elsevier.com/locate/chaos

Spatiotemporal chaos in a conservative Duffing-type system

Eduardo V.M. Reis, Marcelo A. Savi *

Universidade Federal do Rio de Janeiro, COPPE - Department of Mechanical Engineering, Center for Nonlinear Mechanics, Rio de Janeiro, 21.941.972, RJ, Brazil

ARTICLE INFO

Keywords:
Spatiotemporal chaos
Duffing system
Chaos
Nonlinear dynamics
Mechanical vibration
Perturbation

ABSTRACT

This paper deals with an investigation of spatiotemporal chaos in a conservative Duffing-type system governed by a partial differential equation with cubic nonlinearity. Perturbation analysis establishes novel mathematical tools to evaluate different types of dynamical responses in spatiotemporal systems. These tools allow the definition of different Lyapunov exponents: local, convective and mean exponents; being able to provide a local characterization of each kind of response in space. Numerical simulations are carried out showing quasi-periodic and spatiotemporal chaotic responses. An energetic approach is also of concern providing another strategy that allows a proper understanding of system dynamics. In this regard, an energy space is defined from different kinds of energy. A parametric analysis is carried out showing that a higher coupling coefficient present a lower energy dispersion with respect to time.

1. Introduction

Spatiotemporal dynamics has an increasingly scientific and technological relevance, being associated with chemistry, optics, fluid and solid mechanics [1–4]. They can be described either by partial differential equations or by oscillator networks, representing a challenging topic especially when nonlinearities are of concern. Pattern formation, synchronization and spatiotemporal chaos are some kinds of dynamical responses associated with the richness of nonlinear systems.

Among dynamical systems that present spatiotemporal chaos, one should highlight systems modeled by the Ginzuburg–Landau equation [5–7], Kuramoto–Sivashinsky equation [8,9], fluid turbulent flow systems [10–13] and reaction–diffusion systems of relevance in chemistry and biology [14–16]. Metamaterials are another example where spatiotemporal dynamics is of special interest. In general, periodic structures composed by oscillator networks are of concern [17–19]. Fang et al. [20] modeled an acoustic metamaterial using a network of nonlinear oscillators observing bifurcations with energy dispersion and mode interaction phenomena.

Regarding oscillator networks, a paradigmatic example is a system of coupled logistic maps, which are associated with different physical representations that include population dynamics [21–24]. A system composed by a chain of Duffing oscillators is another example that is characterized by cubic nonlinearities [25,26]. Umberger et al. [27] presented a pioneer study of this type of system considering periodic boundary conditions. Chatterjee et al. [28] treated a chain of Duffing oscillators subjected to harmonic excitation, calculating the convective Lyapunov exponents and observing the light-cone boundary during transient period. Musielak et al. [29] studied routes to chaos in a network of Duffing oscillators showing that the increase of the number of degrees of freedom can lead to crisis, instead of period doubling, as the main route to chaos. Romeo and Rega [30] performed a wave propagation analysis.

Several mathematical tools are employed to analyze and characterize the dynamics of complex systems. Chaos diagnosis is an important issue, which has been the objective of several research efforts [31–33]. Lyapunov exponents are one of the most employed tool to characterize chaos. In this regard, one should mention the Lyapunov spectrum obtained from the Gram–Schmidt orthogonalization procedure and covariant Lyapunov vectors [33]. Nevertheless, these procedures need adaptations for spatiotemporal systems [34–37]. Cross and Hohenberg [38] presented an extensive work on the dynamics of spatial extended systems. They employed the Lyapunov spectrum as a tool to evaluate the spatiotemporal dynamics and discussed three characteristic lengths associated with spatiotemporal dynamics: dissipation, excitation and correlation lengths. Shibata [34] proposed mean and local (in time) Lyapunov exponents for spatiotemporal systems based on the first order temporal finite difference method. Kaneko and Deissler [5] proposed the convective Lyapunov exponent, a measure that evaluates the perturbation growth rate along a path in space–time map, showing that there is an optimum path that maximizes the perturbation growth rate. Afterwards, Deissler [6] applied this tool to measure convective chaos in a Ginzburg–Landau model.

This paper deals with the spatiotemporal dynamics of a Duffing-type mechanical system governed by partial differential equations with

* Corresponding author.
E-mail address: savi@mecanica.coppe.ufrj.br (M.A. Savi).

https://doi.org/10.1016/j.chaos.2022.112776
Received 24 January 2022; Received in revised form 27 September 2022; Accepted 1 October 2022

cubic nonlinearity. This system is equivalent to a network of Duffing oscillators [27], being able to represent several physical phenomena such as multiple connected Moon–Holmes beams [39,40] or acoustic metamaterials [41]. A conservative system is of concern which means that dissipation and external excitation are neglected. Novel nonlinear tools are employed to develop the dynamical analysis with focus on spatial dependence and chaos identification. In this regard, one should mention the definition of local and spatial mean perturbations. Local, convective and mean Lyapunov exponents are derived from them, allowing the evaluation of different types of response. An energetic approach is also of concern together with space–time split for the system analysis. Results show that the perturbation growth rate with respect to time depends on the mechanical energy level and on the spatial coupling coefficient. Energetic investigations allow a proper comprehension of some complex behaviors, showing that a higher coupling coefficient present a lower energy dispersion with respect to time.

This manuscript is organized as follows: Section 2 describes the mathematical model of the Duffing-type system, the mathematical tools employed to characterize the dynamical responses and the different kinds of mechanical energy; Section 3 analyzes the equilibrium configurations; Section 4 develops a dynamical analysis showing different kinds of spatiotemporal responses; Section 5 analyzes the dynamical responses using an energetic approach; Section 6 employs mathematical tools based on the perturbation analysis; and, finally, the conclusions are discussed in Section 7.

2. Spatiotemporal Duffing-type system

Duffing oscillator is governed by a differential equation with cubic nonlinearity, named as a tribute for the german engineer Georg Duffing (1861–1944). Throughout the years, Duffing oscillator became vastly investigated due to its complex behavior that includes chaos, and also due to the possibility to describe different physical realizations as hardening/softening stiffness behavior, double-well potential systems, pendular systems, electrical systems, among others. An example of a physical system represented by the Duffing oscillator is the Moon–Holmes beam [39,40], largely employed for energy harvesting purposes.

A spatiotemporal dynamical investigation of a Duffing-type system is of concern, allowing a proper comprehension of the different responses together with their characterization. In this regard, consider a Duffing-type system by assuming the dimensionless displacement u, the spatial coordinate $x \in [0,1]$ and time t. In this regard, the spatiotemporal dynamics is governed by the following partial differential equation (PDE),

$$\ddot{u} = \sigma u'' + \sigma' u' + \frac{1}{2}\left(u - u^3\right) \tag{1}$$

where $\dot{(\,)}$ means partial time derivative $\partial(\,)/\partial t$ and $(\,)'$ denotes spatial partial derivative $\partial(\,)/\partial x$. This system is an extension of the discrete model studied by Umberger et al. [27], considering a continuous spatial dimension. Boundary conditions are assumed to be $u(0,t) = u(1,t) = 0$. Spatial coupling coefficient $\sigma = \sigma(x)$ is space dependent and situations with $\sigma' = 0$ are called reciprocal, being characterized by a spatial symmetrical energy propagation. On the other hand, $\sigma' \neq 0$ stands for nonreciprocal systems, being characterized by an asymmetrical energy propagation [42,43]. The system is spatially decoupled when $\sigma = 0$, a situation where it does not present spatial dependence, being reduced to an oscillator described by ordinary differential equations (ODEs) [26]. Under this assumption, the system has a double well potential, with a bistable behavior associated with three equilibrium points: $(u,v) = (-1,0)$, $(u,v) = (+1,0)$, and $(u,v) = (0,0)$. The first two points are stable while the third is unstable. On the other hand, in the limit $\sigma \to \infty$, there is a rigid spatial attachment with only one possible solution: $u(x,t) = 0$.

2.1. Perturbations

A general form of the dynamical system with spatial dependence can be written as follows:

$$\dot{\mathbf{u}} = f(\mathbf{x}, t, \mathbf{u}, \mathbf{u}', \mathbf{u}'', \mathbf{u}''', \ldots, \mathbf{u}^{(m)}, \mathcal{P}) \tag{2}$$

where $\mathbf{x}$ is the spatial coordinates, t is time, $\mathbf{u} = \mathbf{u}(\mathbf{x},t) \in \mathbb{R}^n$ and $\mathcal{P}$ represents a set of parameters. Let $\bar{\mathbf{u}}$ be a reference solution of the equation of motion and its perturbation $\mathbf{u}_p$, such that $\mathbf{u} = \bar{\mathbf{u}} + \mathbf{u}_p$, and which can be obtained from a linearization of these equations: $\dot{\mathbf{u}}_p = D_{\mathbf{u}} f\, \mathbf{u}_p + \sum_{i=1}^{m} D_{\mathbf{u}^{(i)}} f\, \mathbf{u}_p^{(i)}$, where D is the Jacobian with respect to $\mathbf{u}$.

Therefore, the canonical form of the equations of motion and the perturbation equations for the Duffing-type system are given by

$$\begin{aligned} \dot{u} &= v \\ \dot{v} &= \sigma u'' + \sigma' u' + \frac{1}{2}(u - u^3) \\ \dot{u}_p &= v_p \\ \dot{v}_p &= \sigma u_p'' + \sigma' u_p' + \frac{1}{2}(1 - 3u^2)u_p \end{aligned} \tag{3}$$

with boundary conditions $u(0,t) = u(1,t) = u_p(0,t) = u_p(1,t) = 0$.

The perturbed orbit evolution defines the main characteristic of the system dynamics, since chaotic behavior is characterized by divergent perturbations with respect to the reference orbit while periodic behavior is characterized by convergent perturbed orbits. In order to investigate spatial and temporal perturbation characteristics, two quantities are defined: a local perturbation, ϕ, which is a function of spatial position and time; and an average spatial perturbation, ψ, which is a function of time. Initially, one defines the local perturbation scalar quantity ϕ, as follows

$$\phi(\mathbf{x},t) = \sqrt{\mathbf{u}_p(\mathbf{x},t) \cdot \mathbf{u}_p(\mathbf{x},t)} \tag{4}$$

where $(\,)\cdot(\,)$ represents the dot product.

Spatiotemporal characteristics can be evaluated by evaluating the ϕ on a specific path in the space–time map, expressed by a function $\mathbf{x}(t)$ [5,44,45]. By assuming a linear path, $\mathbf{x}(t) = \mathbf{w}t + \mathbf{x}_0$, for instance, the slope $\mathbf{w}$ can be understood as a path velocity associated with a specific direction. Additionally, it should be pointed out that the limited spatial domain region occupied by a perturbation $\phi(\mathbf{x},t)$ is defined by the perturbation wave packet that is spread along the whole spatial domain as time evolves.

In order to quantify the average spatial perturbation growth with respect to time, the quantity ψ is defined as follows

$$\psi(t) = \sqrt{\frac{\int_V \phi(\mathbf{x},t)^2 \,\mathrm{dV}}{\int_V \phi(\mathbf{x},0)^2 \,\mathrm{dV}}} \tag{5}$$

where V is the spatial domain. On this basis, the following perturbation quantities are defined for the Duffing-type system,

$$\begin{aligned} \phi(x,t) &= \sqrt{u_p(x,t)^2 + v_p(x,t)^2}\,; \\ \psi(t) &= \sqrt{\frac{\int_0^1 u_p(x,t)^2 + v_p(x,t)^2 \,\mathrm{d}x}{\int_0^1 u_p(x,0)^2 + v_p(x,0)^2 \,\mathrm{d}x}} \end{aligned} \tag{6}$$

The estimation of these quantities needs to avoid the divergence of chaotic orbits during numerical simulations. Therefore, it is necessary to normalize the perturbation vector $\mathbf{u}_p$, which is done by assuming new initial conditions for each time step, as schematically showed in Fig. 1. In this regard, the normalization at each t_n, is performed by the average spatial perturbation at this time: $\hat{\mathbf{u}}_p(t_{n+1}) = \mathbf{u}_p(t_{n+1}) / \sqrt{\int_V \langle \mathbf{u}_p(\mathbf{x},t_n), \mathbf{u}_p(\mathbf{x},t_n)\rangle \mathrm{d}V}$.

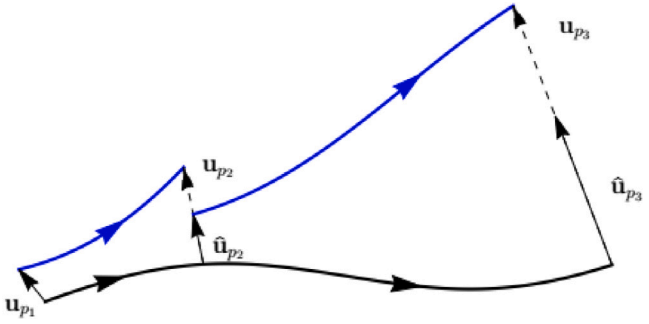

Fig. 1. Schematic picture of the normalization of $\mathbf{u}_p$ at each time step. The black curve stands for a reference orbit $\bar{\mathbf{u}}$ and the blue curve for the perturbed orbit. (For interpretation of the references to color in this figure legend, the reader is referred to the web version of this article.)

Based on the normalization strategy, both ϕ and ψ can be estimated as follows,

$$\begin{aligned}\phi(\mathbf{x},t_n) &= \phi(\mathbf{x},t_0)\prod_{i=1}^{n}\frac{\phi(\mathbf{x},t_i)}{\hat{\phi}(\mathbf{x},t_{i-1})}\\ \psi(t_n) &= \psi(t_0)\prod_{i=1}^{n}\frac{\psi(t_i)}{\hat{\psi}(t_{i-1})}\end{aligned} \tag{7}$$

The perturbation quantities are directly related to the Lyapunov exponents. The local Lyapunov exponent at a specific spatial position is defined from the quantity ϕ. The convective Lyapunov exponent, on the other hand, is estimated by considering the analysis of ϕ that follows a specific path $\mathbf{x}(\mathcal{R},t)$, being $\mathcal{R}$ a parameter that defines the space–time path. Finally, the mean Lyapunov exponent [34] can be estimated from the quantity ψ.

Therefore, the definition of the local and convective Lyapunov exponents can be done by the ratio of the local perturbation logarithm of quantity ϕ over time. Similar definition can be done for the mean Lyapunov exponent using perturbation ψ.

$$\begin{aligned}\lambda_{\text{local}}(\mathbf{x}) &= \lim_{t\to\infty}\frac{1}{t}\log\left(\frac{\phi(\mathbf{x},t)}{\phi(\mathbf{x},0)}\right)\\ \lambda_{\text{conv}}(\mathcal{R}) &= \lim_{t\to\infty}\frac{1}{t}\log\left(\frac{\phi(\mathbf{x}(\mathcal{R},t),t)}{\phi(\mathbf{x},0)}\right)\\ \lambda_{\text{mean}} &= \lim_{t\to\infty}\frac{1}{t}\log\left(\frac{\psi(\mathbf{x},t)}{\psi(\mathbf{x},0)}\right)\end{aligned} \tag{8}$$

One should notice that the local Lyapunov herein defined, λ_{local}, stands for the Lyapunov exponent evaluated locally at a spatial position. Some authors also use this nomenclature for the Finite Time Lyapunov Exponent [33,46], which stands for the Lyapunov exponent defined only locally in time.

Alternatively, the estimation of the Lyapunov exponents can be done by considering a time series regression [47,48]. Therefore, fitting the points $(t,\log(\phi))$ with a basis functions $q_{\text{local}}(t)$ and $q_{\text{conv}}(t)$; and fitting $(t,\log(\psi))$ with the basis function $q_\psi(t)$, the local, convective and mean Lyapunov exponents are defined as follows

$$\begin{aligned}\lambda_{\text{local}}(\mathbf{x}) &= \lim_{t\to\infty}\dot{q}_{\text{local}}(t)\\ \lambda_{\text{conv}}(\mathcal{R}) &= \lim_{t\to\infty}\dot{q}_{\text{conv}}(t)\\ \lambda_{\text{mean}} &= \lim_{t\to\infty}\dot{q}_{\text{mean}}(t)\end{aligned} \tag{9}$$

By considering a linear function q that represents all the three definitions discussed, it is possible to identify the Lyapunov exponents as follows,

$$q(t) = \lambda t + b \tag{10}$$

The evolution of perturbation quantities is employed to characterize spatiotemporal dynamics. In essence, a closed curve in the state space that presents $\lambda_{\text{local}} \leq 0$ characterizes a periodic response in time. If the spatial region presents $\lambda_{\text{local}} = 0$, the system presents a quasi-periodic response in time. Spatiotemporal chaos are characterized by a spatial region with $\lambda_{\text{local}} > 0$ and irregular spatial configuration. If λ_{local} is approximately constant and the same for all spatial domain, then the λ_{mean} can be employed to evaluate the average spatial response, yielding the largest Lyapunov exponent [38].

Similar mathematical tools are employed in the literature to characterize spatiotemporal responses. The Lyapunov spectrum is one of the main tool employed for extended systems, and a continuous set of positive exponents, given by the eigenvalues of the Jacobian matrix, defines spatiotemporal chaos [33,38]. On this basis, Livi et al. [49] stated that in the thermodynamic limit, the Lyapunov spectrum converges when the number of sites in a lattice is increased. Shibata [34] employed the same idea, stating that the order or disorder of spatial patterns is associated with the mean Lyaponuv exponent in time.

In this work, it is adopted λ_{local} to characterize the spatiotemporal dynamics, since it is able to characterize the local response in space, while the Lyapunov spectrum and largest Lyapunov exponent obtained from the Jacobian of the system represent a sort of spatial global average behavior of the system.

2.2. Conservation of mechanical energy

Energy conservation can be established from the integration of the governing equation through a time interval $[t_1,t_2]$ and the whole spatial domain $[0,1]$. Therefore, it is possible to write

$$\int_0^1\int_{t_1}^{t_2}\left[-\ddot{u}+\sigma u''+\sigma' u'+\left(\frac{u}{2}-\frac{u^3}{2}\right)\right]\dot{u}\,\mathrm{d}t\,\mathrm{d}x = 0 \tag{11}$$

After integration by parts and some algebraic manipulation, where it is assumed that $\dot{u}=0$ at $x=0$ and $x=1$ due to boundary conditions, one establishes the conservation of mechanical energy,

$$\left[\int_0^1\left(\frac{1}{2}v^2+\frac{1}{2}\sigma\left(u'\right)^2-\frac{1}{4}u^2+\frac{1}{8}u^4\right)\mathrm{d}x\right]_{t_1}^{t_2} = 0 \tag{12}$$

The mechanical energy conservation preserves volume in state space associated with the following Hamiltonian function obtained as the sum of three kinds of energy, $H = E_K + E_P + E_D$:

$$\begin{aligned}&\text{Kinetic energy}: E_K = \int_0^1\frac{1}{2}v^2\,\mathrm{d}x\\ &\text{Potential energy}: E_P = \int_0^1\frac{1}{2}\sigma\left(u'\right)^2\,\mathrm{d}x\\ &\text{Duffing-type potential energy}: E_D = \int_0^1\left(-\frac{1}{4}u^2+\frac{1}{8}u^4+\frac{1}{8}\right)\mathrm{d}x\end{aligned} \tag{13}$$

Note that the term $1/8$ is added to E_D to assure $E_D \geq 0 \;\;\forall\;\; u$. Moreover, since E_K and E_P are always positive, the mechanical energy is strictly positive for any u and v.

3. Equilibrium configurations

The Duffing-type system has equilibrium configurations that represent steady state solutions, $u = u(x,t) = U(x)$, which means that there is not temporal variation of any variable: $\partial(\,)/\partial t = 0$. Therefore, the equilibrium configurations U_i are obtained solving the following ODE:

$$\sigma U'' + \sigma' U' + \frac{1}{2}(U-U^3) = 0\,; \tag{14}$$

with boundary conditions $U(0) = U(1) = 0$. This boundary value problem can be solved using the shooting method [50]. In this regard, an iterative numerical integration procedure is adopted by assuming $U(0) = 0$ and different trial values of $U'(0)$. Each value of $U'(0)$ is associated with a specific $U(1)$, which defines pairs $\{U'(0),U(1)\}$. By analyzing these pairs, it is possible to build a curve and to identify

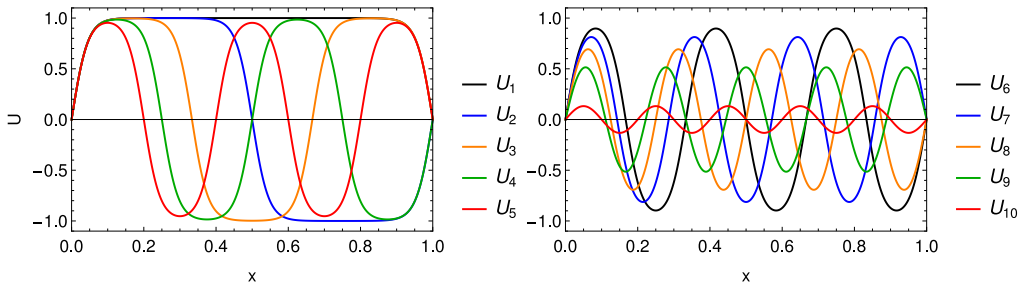

Fig. 2. Equilibrium configurations U_i. (For interpretation of the references to color in this figure legend, the reader is referred to the web version of this article.)

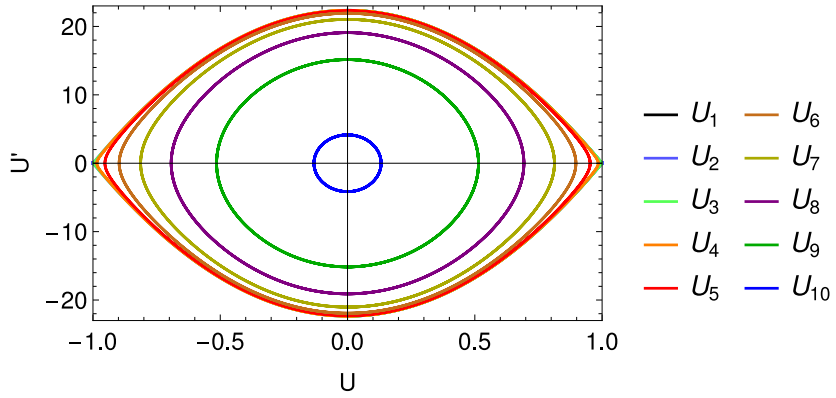

Fig. 3. Equilibrium configurations U_i in state space. (For interpretation of the references to color in this figure legend, the reader is referred to the web version of this article.)

the roots that satisfies the boundary condition $U(1) = 0$. On this basis, eleven different roots are identified. The number of solutions is limited since for $U'(0)$ above a critical threshold, U'_{cr}, it is not possible to satisfy $U(1) = 0$. Hence, only eleven roots are found in the range $U'(0) \in [0, U'_{cr}]$. Fig. 2 shows the equilibrium configurations $U_i (0 \leq i \leq 10)$ with $\sigma = 5\times10^{-4}$ (does not depend on x). Note that subscript i is such that it stands for the total number of local minimum and/or maximum points found in $U_i(x)$. Therefore, $U_0 = 0$ is the trivial solution; U_1 has only one local minimum or maximum points; U_2 has two, and so on.

It is noticeable that as i increases, (a) the amplitude of each configuration decreases and (b) the shape of the curves approaches towards to a harmonic function shape. It is possible to assume that (a) is the cause of (b), since a function with less amplitude yields a lower influence of the nonlinearity of the Eq. (14). Fig. 3 presents phase spaces which shows that as i increases, the equilibrium configuration curves tend to become less sharp at $U = -1$ and $U = +1$, assuming ellipse shapes. Regarding the stability of the solutions, a linear stability analysis shows that all solutions are unstable, except for U_1 that has neutral stability.

Concerning the mechanical energy of each equilibrium configuration U_i, Fig. 4 shows the contribution of each kind of energy to the total mechanical energy. Since U_i requires that $\partial(\,)/\partial t = 0$, by definition $E_K = 0$. For lower energy levels, the total mechanical energy has equal contributions from E_D and E_P. Nevertheless, for higher energy levels, the amplitude of U_i becomes smaller, which makes E_D to increase and, although a higher i yields a higher number of local minimum and/or maximum points, E_P tends to decrease.

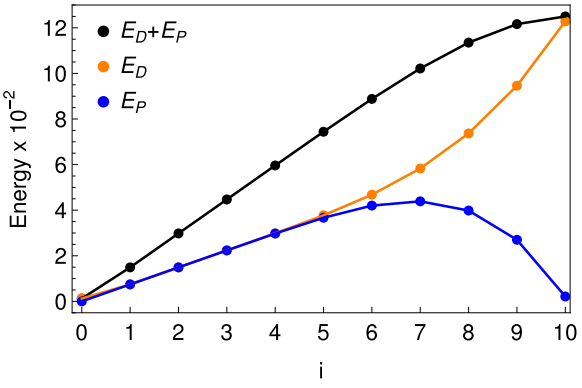

Fig. 4. Potential (blue), Duffing-type potential (orange) and total mechanical (black) energies of U_i. (For interpretation of the references to color in this figure legend, the reader is referred to the web version of this article.)

4. Dynamical analysis

A dynamical analysis is carried out by considering numerical simulations that employs the fourth order finite difference scheme for spatial discretization with 5001 points while time discretization employs the fourth order Runge–Kutta method with a time step of 5×10^{-4}. The dynamical behavior of the Duffing-type system is of concern varying the level of mechanical energy, h, and adopting a constant coupling value. Different values of σ generate quantitatively similar dynamical responses, and therefore, it is adopted $\sigma = 5 \times 10^{-4}$, except when specified otherwise. In addition, initial conditions consider $v(x, 0) = 0$ and $u(x, 0) = \chi \sin(\pi x)$, where χ is a coefficient standing for the amplitude. Different χ were employed for different sought values of h. The only exception takes place for $h = 0.015$, where the initial condition for the displacement employed is given by $u(x, 0) = U_1 + \chi \sin(\pi x)$, i.e., a sine perturbation around the first equilibrium configuration U_1.

Spatiotemporal dynamics is analyzed by considering a space–time split and, therefore, spatial and temporal aspects are investigated separately. This approach can be understood as Poincaré sections considering time evolution of a specific spatial point and, similarly, a spatial evolution for a specific time instant. On this basis, when both spatial and temporal Poincaré sections show irregular responses, the system presents spatiotemporal chaos. On the other hand, when both Poincaré sections responses are regular, a periodic or quasi-periodic spatiotemporal response is achieved.

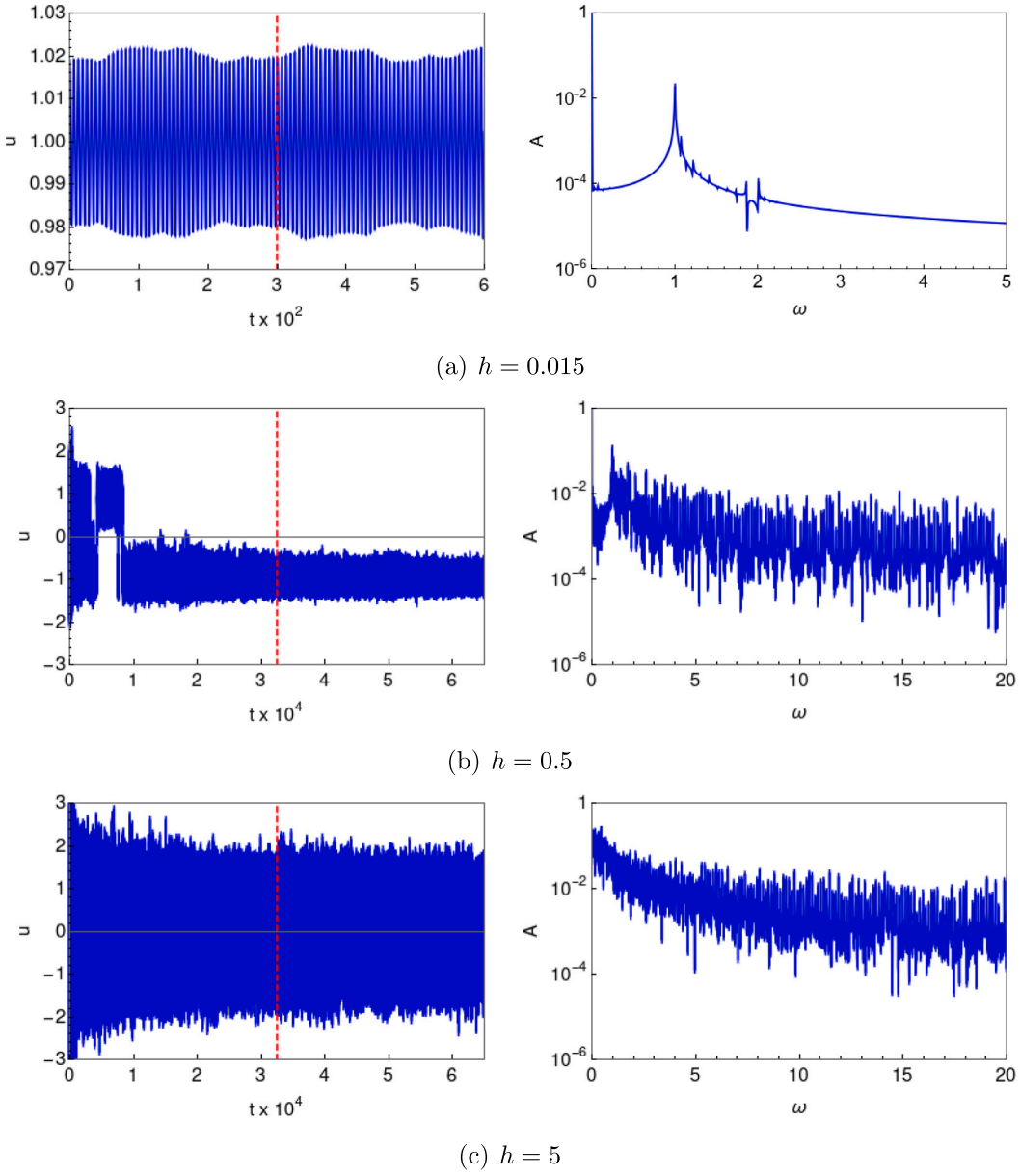

Fig. 5. Time history and its frequency domain analysis at $x = 0.5$ for three different h values. The red lines stand for $t = 300$ (a) and $t = 325 \times 10^2$ ((b) and (c)) where the spatial analysis is performed in Fig. 6.

Initially, temporal analysis is of concern observing dynamical response at a specific space position. Fig. 5 shows the time history at middle spatial position $x = 0.5$ and its respective frequency domain analysis for three distinct energy level values, h: 0.015, 0.5 and 5. The frequency response is based on the Fast Fourier Transform (FFT) that maps $(t, u) \rightarrow (\omega, A)$, where ω is the angular frequency and A is its amplitude. The system response is quasi-periodic for low energy level, $h = 0.015$. This is clearly observed in the frequency domain, whose peaks corresponding to eigenfrequencies of the linear analysis around U_1 are incommensurate. For higher energy levels, temporal evolution presents a chaotic-like response, which can also be observed in the frequency response that is spread over several frequencies presented for both $h = 0.5$ and $h = 5$.

Spatial analysis considers the displacement at a specific time for three different situations (see dashed red lines in Fig. 5): $t = 300$ for $h = 0.015$, and $t = 325 \times 10^2$ for $h = 0.5$ and 5. Moreover, local state spaces are presented showing displacement–velocity (u–v) space at three different space positions during a time window of 10^3 units of time centered in the previous mentioned times. The spatial configuration is presented in Fig. 6 together with its FFT, which maps $(x, u) \rightarrow (\kappa, \Lambda)$, where κ is the wave number (or spatial frequency) and Λ is its amplitude, and local state space is evaluated at three different spatial positions. For low energy level, $h = 0.015$, there is a symmetry with respect to $x = 0.5$, defining a regular regime. Moreover, concerning the local state, one should note they are characterized by a ring with finite thickness, which is typical of quasi-periodic responses. For higher energy levels, $h = 0.5$ and $h = 5$, the spatial configurations are irregular and the spatial frequency domain clarifies this behavior showing a broad wave number distribution. As for the local state space, Poincaré sections indicate a chaotic-like response, characterized by a spread of points in the state space.

On this basis, it is clear that spatiotemporal chaos is an irregular behavior in both time and space. High energy level responses ($h = 0.5$ and $h = 5$) are associated with chaos. On the other hand, low energy level responses ($h = 0.015$) present a regular response in both time and space, defining a quasi-periodic pattern.

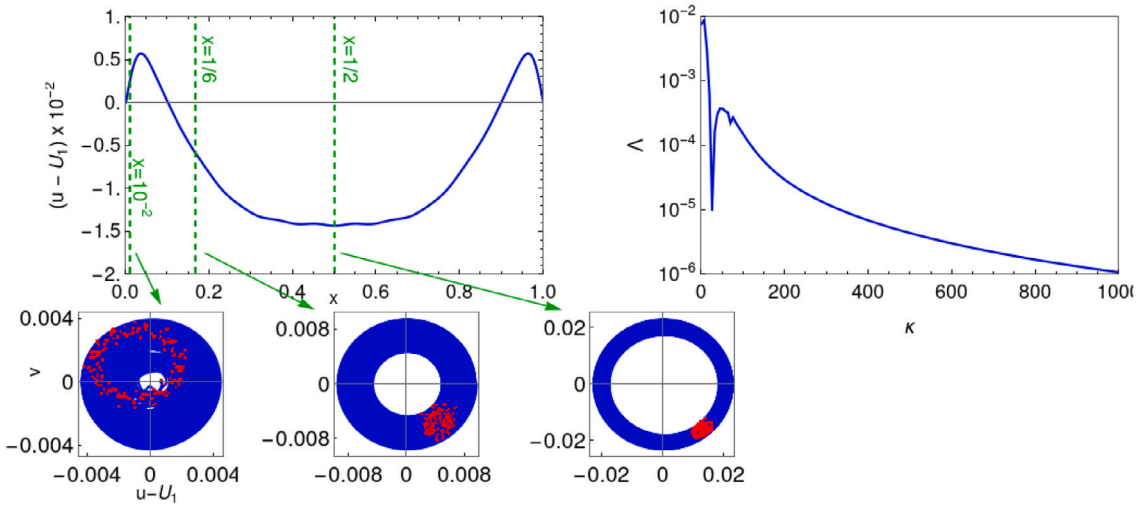

(a) $h = 0.015$

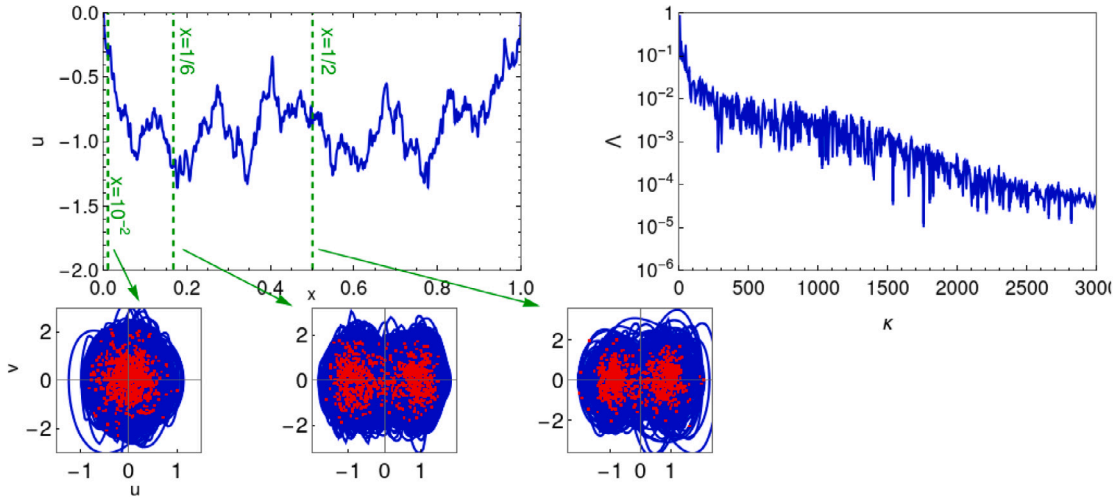

(b) $h = 0.5$

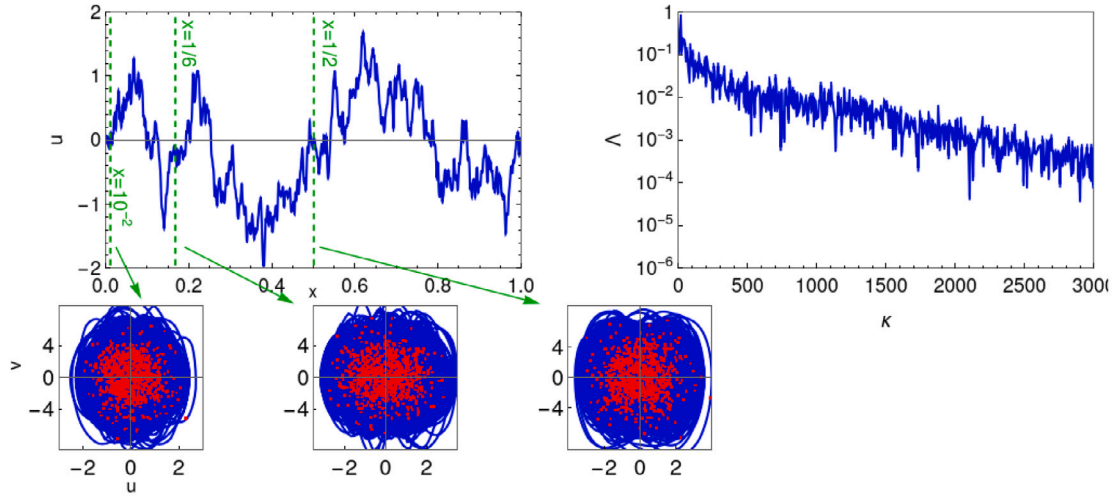

(c) $h = 5$

Fig. 6. Displacement spatial configurations, its respective spatial frequency domain and local state space for three different h values. Red dots stand for the Poincaré section in time whose time interval is the period of the first eigenfrequency around U_1. Spatial configurations are picked up at $t = 300$ (a), $t = 325 \times 10^2$ ((b) and (c)).

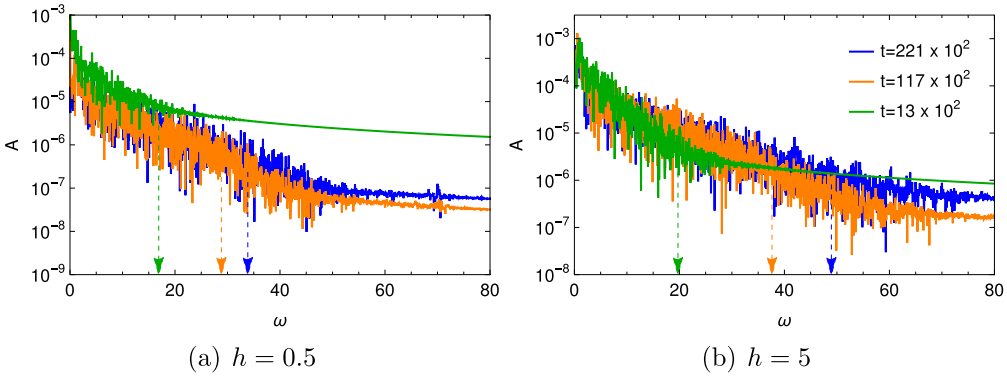

Fig. 7. Frequency analysis of time histories starting at $t = 13 \times 10^2$ (green), 117×10^2 (orange), and 221×10^2 (blue) for a time range of 100. Each respective $\hat{\omega}$ is indicated as a dashed arrow. (For interpretation of the references to color in this figure legend, the reader is referred to the web version of this article.)

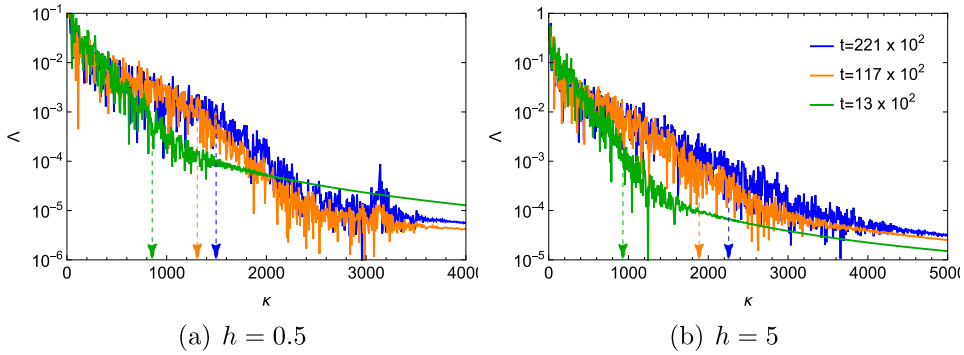

Fig. 8. Spatial frequency analysis of configurations at $t = 13 \times 10^2$ (green), 11.7×10^2 (orange), and 22.1×10^2 (blue). Each respective $\hat{\kappa}$ is indicated as a dashed arrow. (For interpretation of the references to color in this figure legend, the reader is referred to the web version of this article.)

Although the spatial configurations for $h = 0.5$ and $h = 5$ at $t = 325 \times 10^2$ are represented by irregular amplitude distribution of the wave numbers, the initial condition is described by a single wave number. Therefore, as time evolves, the amplitude of higher temporal and spatial frequencies might also increase. In an attempt to quantify how the amplitude on the frequency domain of both temporal and spatial signals spread through higher frequencies, the threshold for temporal $\hat{\omega}(t)$ and spatial $\hat{\kappa}(t)$ frequencies are analyzed. The temporal frequency $\hat{\omega}$ is defined as the frequency where 99% of the area under the Fourier spectrum remains below it. Analogous definition is adopted for the spatial frequency $\hat{\kappa}$. On this basis, the following conditions are adopted

$$\begin{aligned} \int_0^{\hat{\omega}} \Lambda(\omega)\,\mathrm{d}\omega &= 0.99 \int_0^{\infty} \Lambda(\omega)\,\mathrm{d}\omega \\ \int_0^{\hat{\kappa}} \Lambda(\kappa)\,\mathrm{d}\kappa &= 0.99 \int_0^{\infty} \Lambda(\kappa)\,\mathrm{d}\kappa \end{aligned} \tag{15}$$

Fig. 7 presents amplitude evolution through frequency for two levels of energy, $h = 0.5$ and $h = 5$. The FFT is performed considering a time range of 100 units of dimensionless time and the beginning of each time range is $t = 13 \times 10^2$, 117×10^2 and 221×10^2. The dashed arrows indicate the value of $\hat{\omega}$ for each case. Note that $\hat{\omega}$ increases for time histories with bigger initial time, indicating an irregular spread over higher frequencies as time goes by. Correspondingly, Fig. 8 depicts the FFT of the spatial configuration at the same time instants. Note the increase of $\hat{\kappa}$ for spatial configurations taken at bigger time instants.

The next step of the analysis is the evaluation of both $\hat{\omega}$ and $\hat{\kappa}$ as a function of time. This is done in order to investigate if the displacement in both space and time spreads towards higher frequencies. In this regard, a constant growth of both quantities indicates spatiotemporal chaos. Fig. 9 presents the time evolution of both $\hat{\omega}$ and $\hat{\kappa}$ showing that both quantities constantly grow with respect to time when the system presents chaotic behavior. It suggests that energy is constantly being transferred from large temporal and spatial scales to smaller ones. At any time, bigger h yields bigger $\hat{\omega}$ and $\hat{\kappa}$. Additionally, neglecting some initial transient response, the growth follows a linear trend with a slope that depends on h. On this basis, a linear function is employed using the least square method to fit data from Fig. 9 for $t > 2 \times 10^4$, and its slope can measure temporal and spatial irregularities growth rate, being able to characterize the dynamical response. Therefore, if one employs $\hat{\omega}(t) = \theta_t t + \delta_t$ and $\hat{\kappa}(t) = \theta_s t + \delta_s$, θ_t and θ_s are the temporal and spatial slopes, respectively, which yields for the spread rate of temporal and spatial frequencies. The higher the magnitude, the higher is the spread rate.

Fig. 10a presents θ_t for different values of h considering two different values of the coupling coefficient σ. For $\sigma = 5 \times 10^{-4}$, it is noticeable that θ_t increases as h increases up to $h \approx 2$. For higher values of h, θ_t is almost constant. On the other hand, for $\sigma = 5 \times 10^{-3}$, θ_t grows constantly as h increases. Note that in the limit $\sigma \to \infty$ the system becomes spatially fully coupled and it is expected a zero slope, since Eq. (1) yields to $u'' \to 0$ and, due to boundary conditions, $u \to 0$. Therefore, there is not a frequency spread.

5. Energetic analysis

An energetic analysis is now in focus considering the different kinds of energy involved in the system dynamics: E_K, E_P, E_D. Initially, Fig. 11 presents the evolution of the energy quantities through time for $h = 0.5$, representing the average curve by dashed black lines, which shows that the initial transient time previously mentioned in Fig. 5 is characterized by an increase of the mean oscillation of both E_K and E_P and by the decrease of the mean oscillation of E_D. Therefore, there is a transfer of energy from E_D to E_K and E_P through time. The growing average of E_K and E_P are linked with the positive rate of both θ_t and

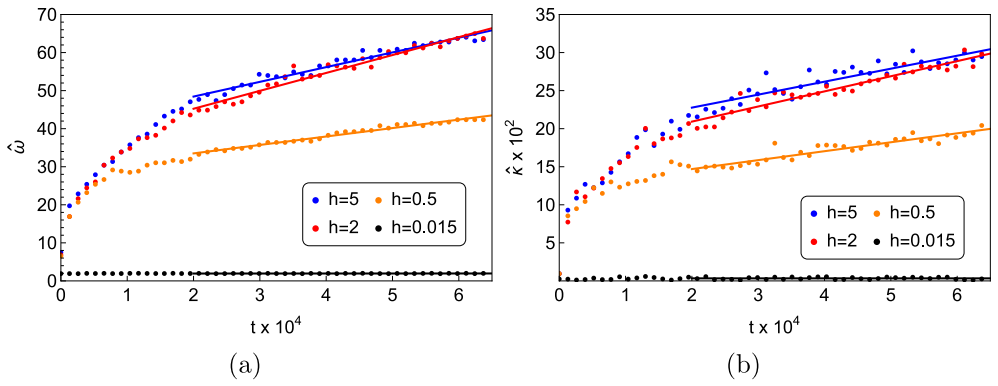

Fig. 9. $\hat{\omega}$ (a) and $\hat{\kappa}$ (b) along time for several h values. The straight lines stand for the linear fitting using the least square method.

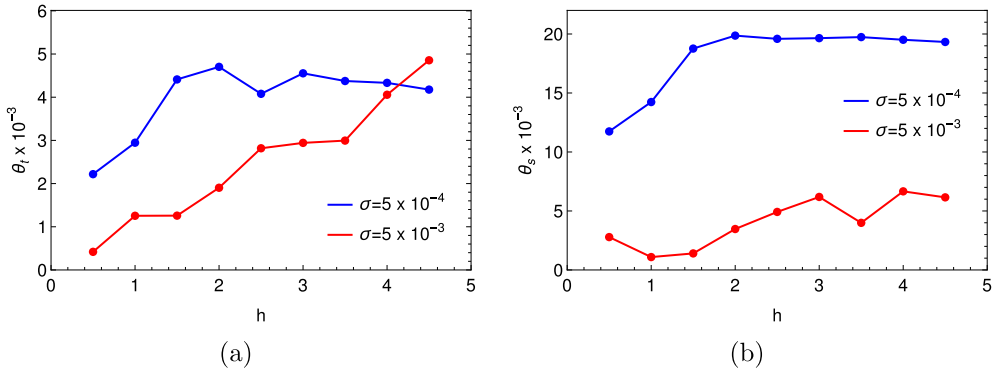

Fig. 10. Slope θ_l (a) and θ_s (b) as a function of h. (For interpretation of the references to color in this figure legend, the reader is referred to the web version of this article.)

θ_s. Therefore, the initial transient time is associated with a higher E_D, followed by its constant average decrease.

An interesting alternative to observe energy issues is from a 3D energy space where each axis defines a kind of energy, which allows the evaluation of the energy distribution. It is considered a normalization of the energy values with respect to the total energy level h, as follows:

$$E_K^* = \frac{E_K}{h}, \qquad E_P^* = \frac{E_P}{h}, \qquad E_D^* = \frac{E_D}{h} \tag{16}$$

Therefore, $E_K^* + E_P^* + E_D^* = 1$ and $(E_K^*, E_P^*, E_D^*) \geq (0,0,0)$ (see Eq. (13)), which turns out that the energy distribution must lie on a plane in the positive quadrant of the energy space, according to Fig. 12.

Based on this idea, the subspace $E_P - E_K$ is considered to be representative of the system dynamics. Fig. 13 shows the energy distribution in this subspace for $h = 0.5$, highlighting the isolines of constant E_D^*. An interesting strategy for visualization is to characterize an energetic boundary built by considering a surface defined by the density of points using a Gaussian surface employing the least square method. In this regard, the energetic boundary is defined as the intersection between the Gaussian surface and a plane parallel to the $E_P - E_K$ plane, where 98% of the volume beneath the Gaussian surface remains within the closed curve. In other words, the energetic boundary is an enclosed curve that contains 98% of the points that characterizes an energy distribution in the subspace $E_P - E_K$. It should be pointed out that Fig. 13 also presents the energetic boundary (red curve).

The influence of the energy level h in system dynamics is now analyzed employing this energetic approach. Fig. 14 presents the energetic boundaries for three energy levels and for two different coupling parameter σ. Note that as h increases, the energetic boundary tends to be closer to the isoline $E_D^* = 0$, which means that a smaller fraction of h is due to E_D^*. On the other hand, both E_K^* and E_P^* reach higher fractions of the total mechanical energy, which means that the contribution of E_K^* and E_P^* become more relevant than E_D^* for situations with bigger mechanical energy level. Moreover, a higher value of the coupling coefficient implies in more dispersion, being characterized by a growth of the area within the energetic boundary. Finally, it is also noticeable that the area within energetic boundaries is proportional to the energy level. Fig. 15 presents the area within energetic boundaries as a function of h showing that the area decays as h increases, indicating less energy dispersion.

6. Perturbation analysis

This section evaluates the system dynamics from the perspective of perturbation evolution. The perturbation initial condition is a bell shaped function centered in the middle of the domain that yields $\psi(0) = 1$. In this regard, it is assumed that $u_p(x,0) = A_p \exp[-100(x-0.5)^2]$ and $v_p(x,0) = 0$ where $A_p = 2.825$. It is worthwhile to mention that, despite the bell shaped function never vanishes in any part of the domain, ϕ is of the order $O(10^{-10})$ in domain boundaries, which is assumed to satisfy boundary conditions. In order to evaluate the spatial distribution of the perturbation, Fig. 16 presents ϕ in the space–time map for different energy levels represented by h: 0.015, 0.5 and 5. The perturbation boundary is defined as the outer isoline given by $\phi = 10^{-1}$, being presented for each simulation as a black dashed line. Note that the initial perturbation is dispersed through space, approximately keeping its order of magnitude as time evolves for the situation with $h = 0.015$, which means that ϕ does not grow. Nevertheless, simulations with $h = 0.5$ and $h = 5$ show a growing ϕ.

The regular dynamics for $h = 0.015$ and irregular dynamics for $h = 0.5$ and 5 are observed in phase space diagrams presented in Fig. 17 for $x = 0.2$ and $x = 0.55$. Note that a quasi-periodic behavior is

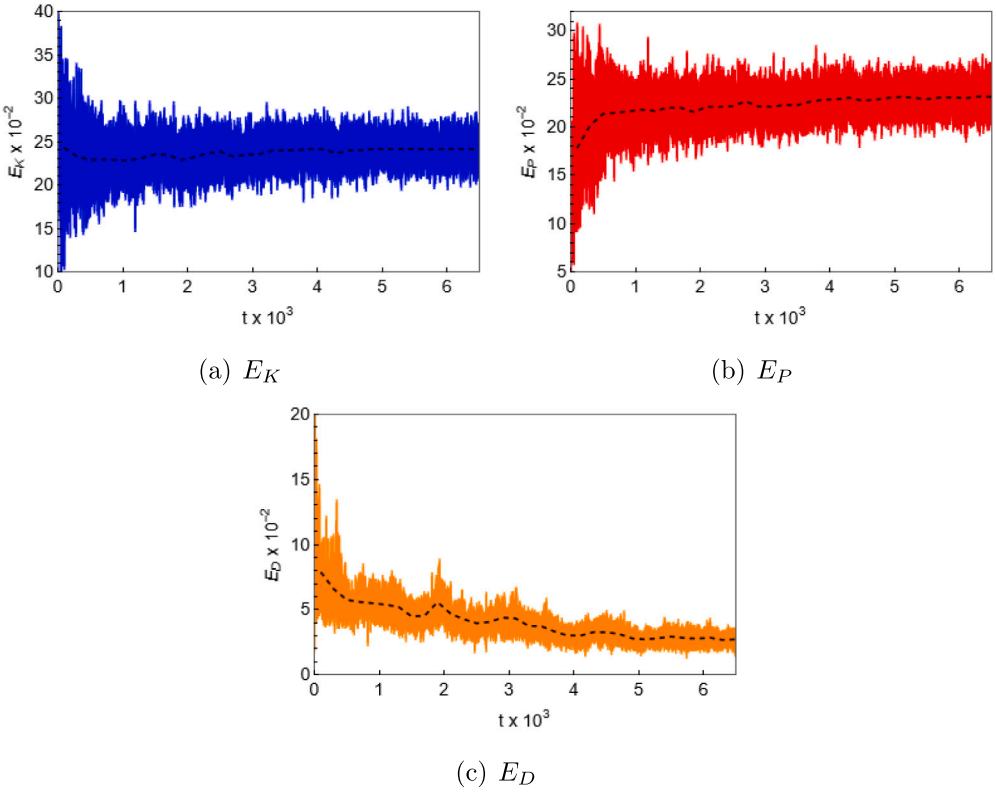

Fig. 11. Energy evolution evaluated from different kinds of energy with a energy level represented by $h = 0.5$. Dashed black lines standing for the average curve for each plot.

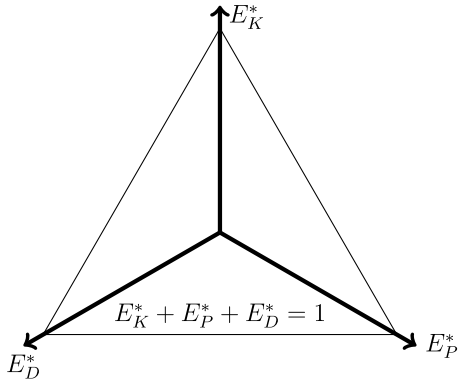

Fig. 12. 3D energy space.

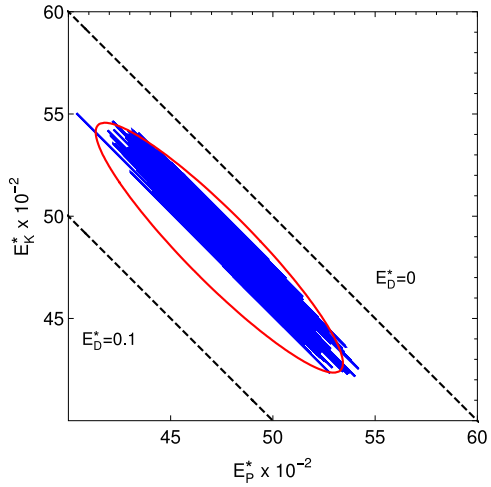

Fig. 13. Energy subspace for $h = 0.5$ (blue region) and energetic boundary (red curve). Dashed lines stand for isolines of constant E_D^*.

observed for low energy level, $h = 0.015$, and a more complex response is occurring for high energy levels, $h = 0.5$ and $h = 5$. Moreover, it is noticeable the bigger amplitudes for the diagram at $x = 0.5$ in contrast of the smaller amplitudes at $x = 0.2$ since it is closer to the boundary.

Once the perturbation reaches the boundaries, it bounces back and keeps oscillating with a constant growing amplitude all over the domain, generating rich spatiotemporal dynamics. This kind of behavior is the signature of ϕ for a spatiotemporal chaos. These two situations are similar concerning the type of perturbation response, and all other simulations for different values of h between 0.5 and 5 have the same trend. Finally, it is noticeable that the perturbation boundaries for the cases with $h = 0.5$ and 5 traveled faster than the case with $h = 0.015$, reaching the spatial domain limits in a faster way.

In order to evaluate the evolution of the local perturbation along different spatial positions, Fig. 18 shows ϕ at three different positions: $x = 10^{-2}$, $1/6$ and $1/2$. Note that, ϕ has always the smaller value at $x = 10^{-2}$ and the evolution of the local perturbation follows the same trend for all spatial positions. For the quasi-periodic response, the growth is not observed. On the other hand, an exponential growth is observed for all spatial domain, except at the boundaries, when the response is chaotic.

Based on this, the perturbation of the high energy levels behavior spreads and grows approximately uniformly through the spatial domain. Therefore, one can employ the perturbation ψ to quantify the growth rate of the average spatial perturbation. In this regard, Fig. 19 presents the evolution of $\log(\psi)$ for different energy levels h, showing that chaotic responses have the growth rate of ψ that is approximately the same regardless the value of h. After the transient period, smaller

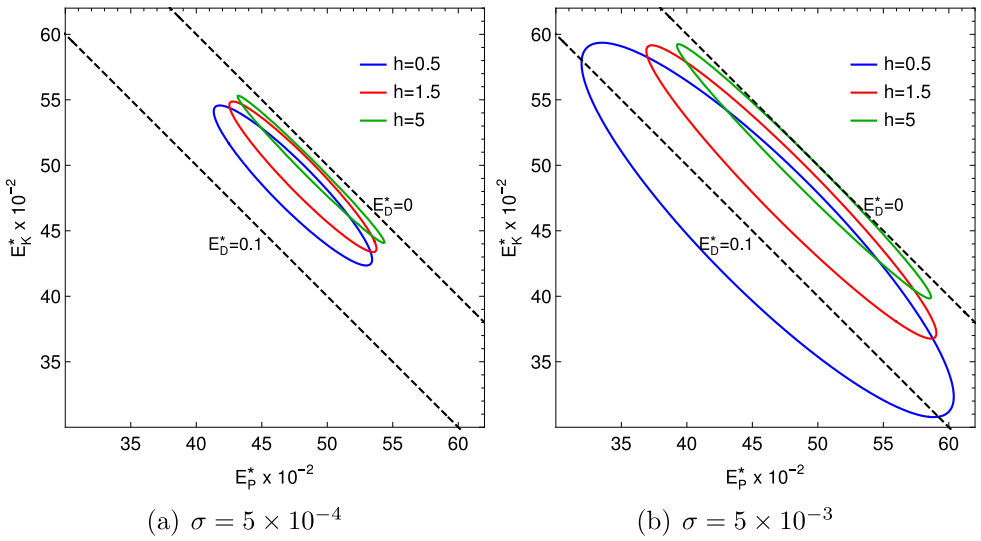

Fig. 14. Energetic boundaries for $h = 0.5$ (blue), $h = 1.5$ (red) and $h = 5$ (green). (For interpretation of the references to color in this figure legend, the reader is referred to the web version of this article.)

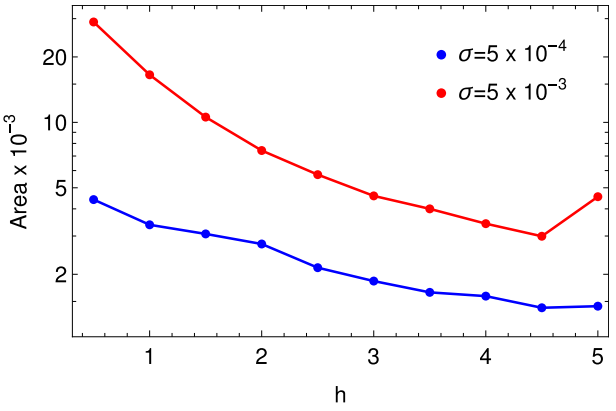

Fig. 15. Energetic boundary area for $\sigma = 5 \times 10^{-4}$ (blue) and $\sigma = 5 \times 10^{-3}$ (red). (For interpretation of the references to color in this figure legend, the reader is referred to the web version of this article.)

h yields smaller growth rate, and there is not a growth rate for the quasi-periodic solution.

By assuming the transient period of 2×10^4 long that is neglected, one employs a linear basis function to fit $(t, \log(\psi))$ data using the least square method. The smallest R^2 statistical fitting coefficient is 0.986. The mean Lyapunov exponent is given by the slope of q_ψ at the limit $t \to \infty$, as previously stated by Eq. (9). Based on that, Fig. 20 presents λ_{mean} for different energy levels h showing that bigger energy levels yield to bigger λ_{mean}.

6.1. Perturbation through specific paths

This section treats the perturbation considering the growth and spread in space–time. One of the tools employed is the evaluation of the convective Lyapunov exponent along different paths in the space–time map. Each path is characterized by a slope or velocity. Once again, the perturbation initial condition is described by a Gaussian bell shaped centered at the middle of the domain. Two different coupling characteristics are analyzed [42,43]: reciprocal system, characterized by a constant spatial coefficient; nonreciprocal system, defined by a coupling coefficient with spatial gradient. In this regard, two functions are adopted: $\sigma_1 = 10^{-7}$ - reciprocal system; and $\sigma_2(x) = \sigma_1 + 98(x - 0.5)10^{-5}$ - nonreciprocal system. Note that the order of magnitude of σ was reduced from the previous analyses. It is also noticeable that $\sigma_1 = \sigma_2$ at $x = 0.5$, being $\sigma_2 > \sigma_1$ for $x > 0.5$.

The first aspect to be concerned regards to the evolution of the perturbation boundary in the space–time map. As previously stated, the perturbation boundary is defined as the outer isoline standing for $\phi = 10^{-1}$, which travel towards spatial domain limits ($x = 0$ and $x = 1$). In order to avoid influence of the boundary condition, simulations are interrupted when perturbation boundaries reaches $x = 0.07$ or $x = 0.93$, whatever takes place first. In other words, when $\phi(0.07, t) \geq 10^{-1}$ or $\phi(0.93, t) \geq 10^{-1}$.

Fig. 21 presents the perturbation boundaries for σ_1 and $\sigma_2(x)$ with $h = 1$, showing wave fronts that define a perturbation wave packet that spreads in space as time evolves. For the reciprocal system (σ_1), perturbation wave fronts travel symmetrically in the negative and positive directions of x axis. On the other hand, nonreciprocal system ($\sigma_2(x)$) presents an asymmetric propagation where the perturbation wave fronts travel faster in the positive direction when compared with the negative direction of x axis. Finally, the evolution of the perturbation boundaries does not alter significantly for higher values of h.

The evaluation of the local perturbation evolution along different paths in the space–time map is now of concern. In this regard, $\phi(x(w,t),t)$ is evaluated assuming a linear path: $x(w,t) = wt + x_0$, where w is the path slope or velocity. Different scenarios are evaluated by considering the following equation,

$$x_j(w_i, t) = w_j t + x_0 \tag{17}$$

where $x_0 = 0.5$ and $w_j = 10^{-2}\left[\frac{(j-1)}{420} - \frac{1}{21}\right]$, with $j = 1, 2, \ldots, 41$. These paths are represented by gray lines in Fig. 21, and paths heading towards the negative direction of x axis are the ones with $1 \leq j < 21$ and otherwise for $21 < j \leq 41$. Besides, $j = 21$ yields a path parallel to the time axis. This analysis is a novel method to evaluate the evolution of local perturbation along different paths where the growth rate furnishes the convective Lyapunov exponent [6,45].

Fig. 22 shows ϕ against time for several w_j and $h = 1$. Note that all paths bend towards the negative direction of spatial axis. For w_j smaller than the perturbation wave front towards negative direction, ϕ decreases with respect to time. In addition, the decreasing rate is bigger for greater differences between w_j and the perturbation boundary wave front. Nevertheless, for a path that remains inside wave packet domain, ϕ grows with respect to time. The evolution of ϕ along path defined by w_9 velocity and with $\sigma_2(x)$ is characterized by an increase of the

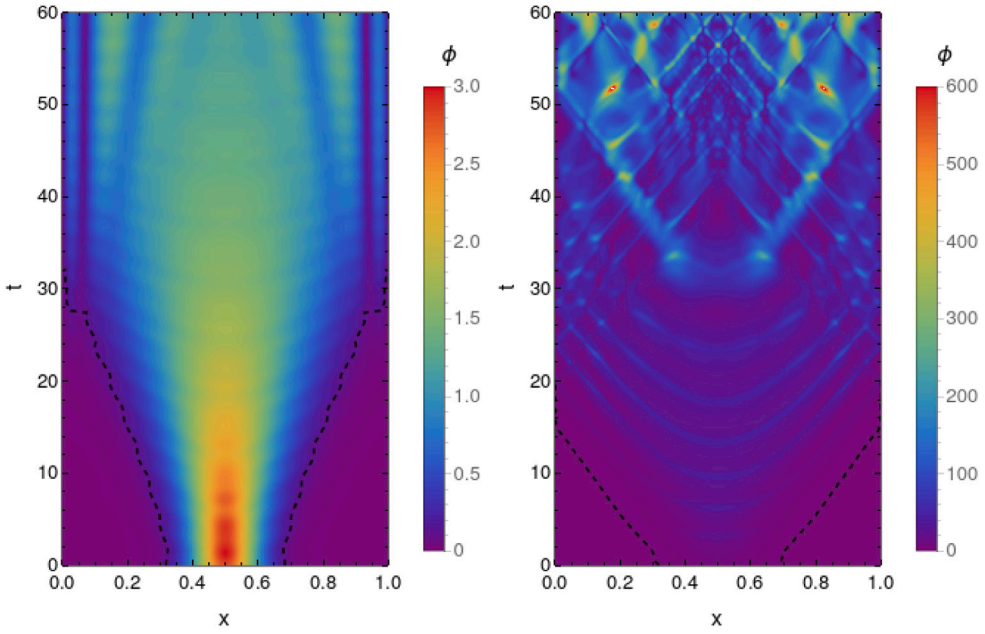

(a) $h = 0.015$ (b) $h = 0.5$

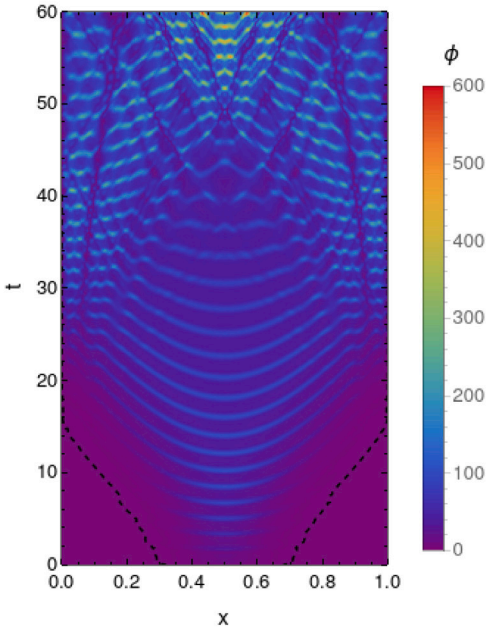

(c) $h = 5$

Fig. 16. Spread of ϕ in the space–time map for three different h values. The black dashed lines stand for the perturbation boundary, herein defined as the outer isoline with $\phi = 10^{-1}$.

perturbation magnitude followed by its decrease. This occurs due to the non constant perturbation wave front propagation velocity. During an initial period of time, the respective path remains within the perturbation wave packet region. Due to the non constant velocity of the perturbation wave front propagation, the path crosses the boundary of perturbation, leaving behind the perturbation wave packet and leading ϕ to drop. This phenomenon is illustrated in Fig. 23. The threshold time where the trajectory path overlapped the perturbation wave front occurs at $t = 752.84$, highlighted by a blue arrow.

Paths that are within wave packet have a divergent trend of $\phi(x(w,t),t)$ and, therefore, it is interesting to compare the influence of path velocity on the growth rate. In this regard, the least square method is employed to fit $(t, \log(\phi))$ data considering a linear function: $q_{\text{conv}}(t) = \lambda_{\text{conv}} t + b$. In order to avoid transient effects, the first 300 units

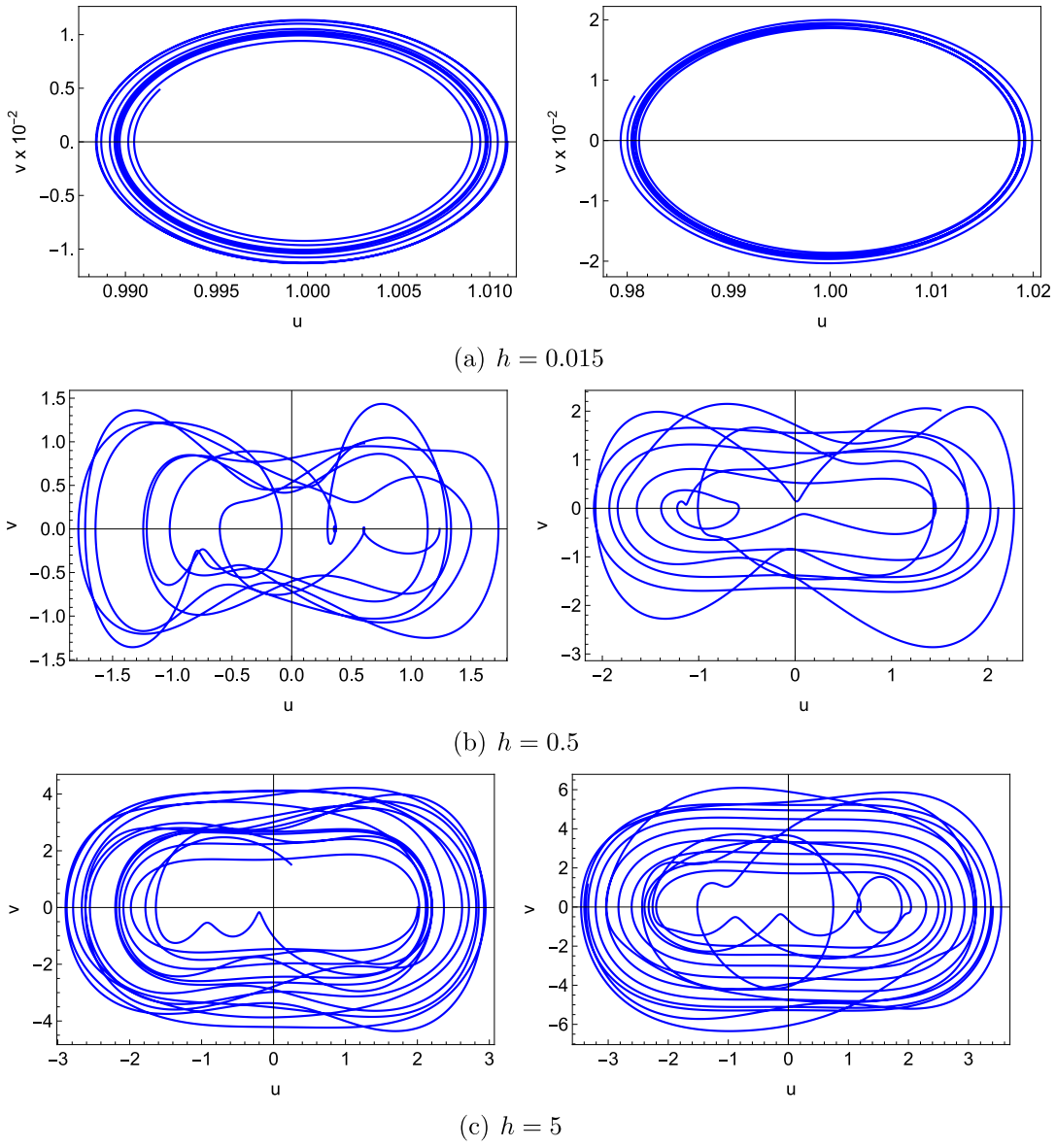

Fig. 17. Phase space diagram at $x = 0.2$ (left column) and $x = 0.5$ (right column) obtained with $0 \leq t \leq 60$.

of dimensionless time are neglected. Fig. 24 shows λ_{conv} values for three energy levels h, considering both reciprocal σ_1 and nonreciprocal $\sigma_2(x)$ systems. Note that, regardless the σ, the convective Lyapunov exponent seems to be independent of the energy level h for spatiotemporal chaotic responses. On the other hand, the quasi-periodic response with $h = 0.015$ presented $\lambda_{\text{conv}} = 0$ through all paths, as expected. Moreover, λ_{conv} is approximately symmetric with respect to the null velocity $w = 0$ path for the reciprocal system σ_1 and symmetry discrepancies are due to transient effects, tending to be smaller for longer simulations. On the other hand, this symmetry is broken for the nonreciplorcal system with coupling parameter $\sigma_2(x)$.

7. Conclusions

This paper deals with the spatiotemporal dynamics of a conservative Duffing-type system governed by a partial differential equation with cubic nonlinearity, which is equivalent to a network of Duffing oscillators. Duffing-type systems represent many physical systems such as multiple connected Moon–Holmes beams, vastly employed for energy harvesting proposes. In this regard, the findings of this article can be employed to improve the design of energy harvesting devices. A general spatiotemporal dynamics is investigated, presenting tools for the proper characterization of different responses. Among the employed tools, it should be highlighted: spatial and temporal Poincaré sections, an energetic analysis and a novel perturbation approach. Numerical simulations are carried out considering finite difference for spatial discretization and fourth-order Runge–Kutta method for time integration. Steady state equilibrium configurations are evaluated considering a time independent boundary value problem, which defines eleven equilibrium configurations. Different energy levels are investigated assuming a singular sine shape function as initial condition. Regular and irregular patterns are possible in space and time depending on the energy level. The analysis is performed by considering a space–time split. Fast Fourier Transform for either space or time is performed, showing that spatiotemporal chaos is characterized by a spread over

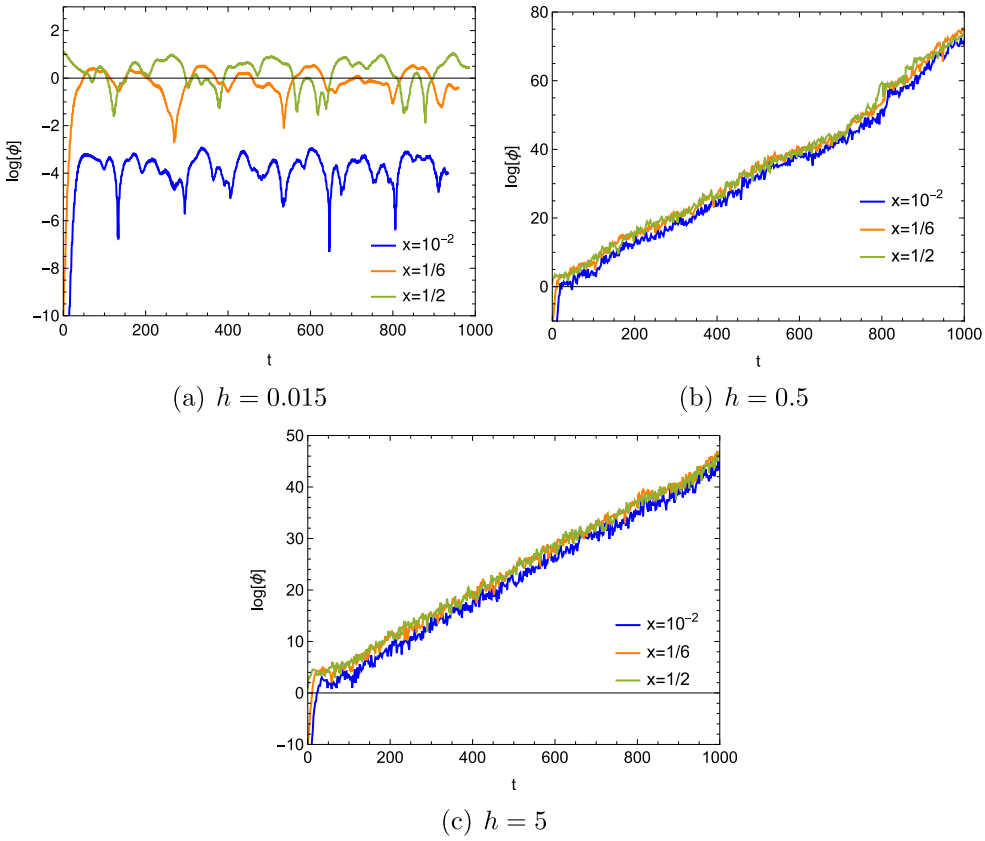

Fig. 18. Local perturbation ϕ evolution at three spatial positions and for three different values of h. (For interpretation of the references to color in this figure legend, the reader is referred to the web version of this article.)

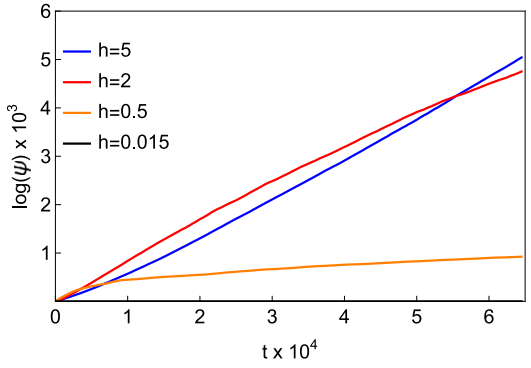

Fig. 19. ψ along time for several values of h. ψ values for $h = 0.015$ did not grow and remained oscillating around 1. (For interpretation of the references to color in this figure legend, the reader is referred to the web version of this article.)

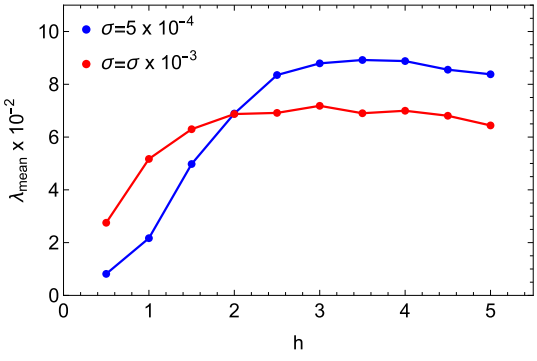

Fig. 20. Mean Lyapunov exponent λ_{mean} against h for two different coupling parameters σ. (For interpretation of the references to color in this figure legend, the reader is referred to the web version of this article.)

temporal and spatial frequencies, indicating that energy is being constantly transferred from larger temporal and spatial scales to smaller ones.

Energetic analysis is performed considering the total mechanical energy as kinetic, potential and Duffing-type potential energies, defining an energy space where a Gaussian surface is employed to characterize the energy distribution. The least square method is employed to build this surface that is useful for a proper comprehension of the system dynamics. Conclusions point that responses with higher energy levels have a less fraction of Duffing-type potential energy as well as a higher portion of both kinetic and potential energies.

Perturbation analysis allows the definition of new mathematical tools employed to characterize spatiotemporal dynamics, including spatiotemporal chaos. The main difference from established tools, such as the Lyapunov exponent spectrum, lies on the fact that they are able to define the type of response locally in space. These quantities are based

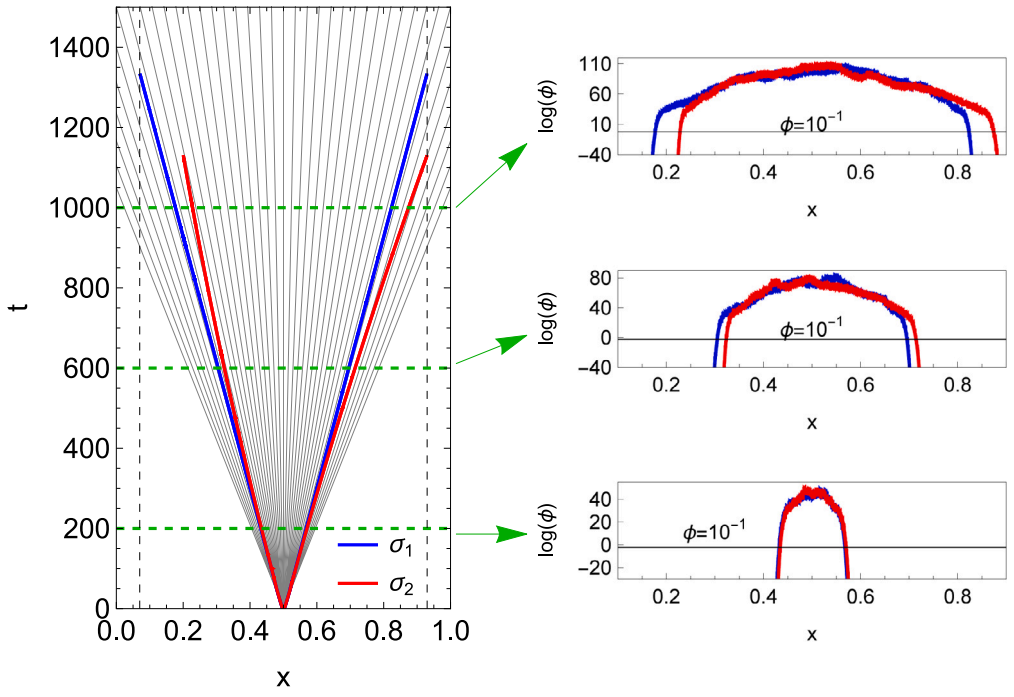

Fig. 21. Perturbation boundaries for $h = 1$ (outer isoline with $\phi = 10^{-1}$) for σ_1 (blue) and $\sigma_2(x)$ (red). The gray lines stand for the 41 different linear paths given by Eq. (17) and vertical dashed lines stand for $x = 0.07$ and $x = 0.93$. (For interpretation of the references to color in this figure legend, the reader is referred to the web version of this article.)

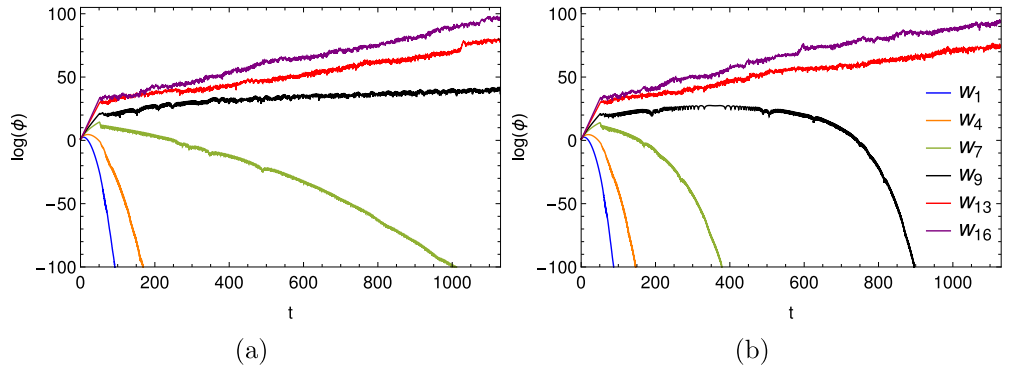

Fig. 22. Growth evolution through time represented by $\log(\phi)$ for $h = 1$ and several paths characterized by w_j and for σ_1 (a) and $\sigma_2(x)$ (b).

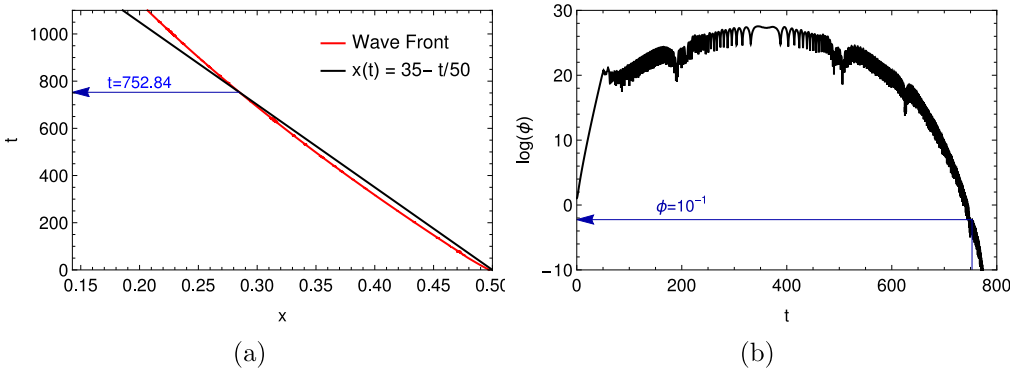

Fig. 23. Perturbation wave front towards negative direction and the path with $w_9 = -1/3500$ in the space–time map (a) and local perturbation $\phi(x(w_9, t), t)$ in time domain. Results for $h = 1$ and $\sigma_2(x)$. (For interpretation of the references to color in this figure legend, the reader is referred to the web version of this article.)

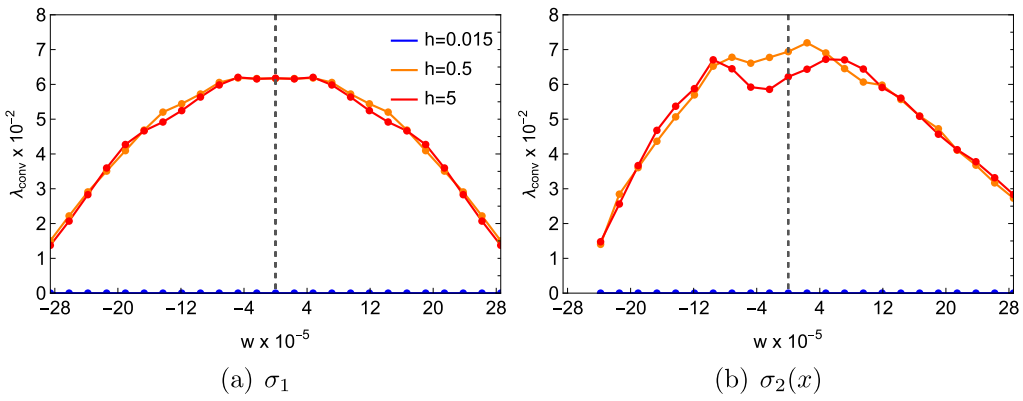

Fig. 24. Comparison of convective Lyapunov exponent, λ_{conv}, for σ_1 (a) and $\sigma_2(x)$ (b). (For interpretation of the references to color in this figure legend, the reader is referred to the web version of this article.)

on Lyapunov exponents: local, convective and mean. The evolution of Gaussian initial perturbation is analyzed showing that it grows in both space and time continuously, which characterizes an irregular pattern associated with spatiotemporal chaos. Besides, it is shown that the mean Lyapunov exponent is strictly related to the mechanical energy. Perturbation evolution through a path in space–time map is employed to estimate the convective Lyapunov exponent. Nonreciprocal systems with positive spatial gradient presents the largest convective Lyapunov exponent for paths bending towards the negative direction of the spatial domain.

CRediT authorship contribution statement

Eduardo V.M. Reis: Conceptualization, Methodology, Software, Validation, Formal analysis, Investigation, Writing. **Marcelo A. Savi:** Conceptualization, Methodology, Software, Validation, Formal analysis, Investigation, Supervision, Writing – reviewing.

Data availability

Data will be made available on request.

Acknowledgments

The authors would like to acknowledge the support of the Brazilian agencies CNPq, CAPES and FAPERJ.

References

[1] Reingruber J, Holcman D. Diffusion in narrow domains and application to photo-transduction. Phys Rev E 2009;79(3):1–4. http://dx.doi.org/10.1103/PhysRevE.79.030904.
[2] Ng J, Dubljevic S. Optimal boundary control of a diffusion-convection-reaction PDE model with time-dependent spatial domain: Czochralski crystal growth process. Chem Eng Sci 2012;67(1):111–9. http://dx.doi.org/10.1016/j.ces.2011.06.050.
[3] Reis EVM, Sphaier LA, Nunes LCS, de B. Alves LS. Dynamic response of free span pipelines via linear and nonlinear stability analyses. Ocean Eng 2018;163(January 2017):533–43. http://dx.doi.org/10.1016/j.oceaneng.2018.06.002.
[4] Reis EVM, de B. Alves LS. Convective and absolute instabilities induced by viscous dissipation in the thermocapillary convection with through-flow. J Heat Transfer 2021;143(5):052601. http://dx.doi.org/10.1115/1.4050312.
[5] Deissler RJ, Kaneko K. Velocity-dependent Lyapunov exponents as a measure of chaos for open-flow systems. Phys Lett A 1987;119(8). http://dx.doi.org/10.1016/0375-9601(87)90581-0.
[6] Deissler RJ. Spatially growing waves, intermittency, and convective chaos in an open-flow-system. Pysica 25D 1987;233–60. http://dx.doi.org/10.1016/0167-2789(87)90103-5.
[7] Van Gorder RA, Krause AL, Planella FB, Burton AM. Coupled complex Ginzburg–Landau systems with saturable nonlinearity and asymmetric cross-phase modulation. Ann Physics 2018;396:397–428. http://dx.doi.org/10.1016/j.aop.2018.07.003.
[8] Gotoda H, Pradas M, Kalliadasis S. Nonlinear forecasting of the generalized kuramoto-sivashinsky equation. Int J Bifurcation Chaos 2015;25(5):1–19. http://dx.doi.org/10.1142/S0218127415300153.
[9] Budanur NB, Cvitanović P. Unstable manifolds of relative periodic orbits in the symmetry-reduced state space of the Kuramoto–Sivashinsky system. J Stat Phys 2017;167(3–4):636–55. http://dx.doi.org/10.1007/s10955-016-1672-z.
[10] Ruelle D, Takens F. On the nature of turbulence. Les Rencontres Phys-Math Strasbourg-RCP25 1971;12:1–44. http://dx.doi.org/10.1007/BF01893621.
[11] Manneville P. Laminar-turbulent patterning in transitional flows. Entropy 2017;19(7):316. http://dx.doi.org/10.3390/e19070316.
[12] Tokami T, Hachijo T, Miyano T, Gotoda H. Spatiotemporal dynamics of a buoyancy-driven turbulent fire. Phys Rev E 2020;101(4):042214. http://dx.doi.org/10.1103/PhysRevE.101.042214.
[13] Kobayashi W, Gotoda H, Kandani S, Ohmichi Y, Matsuyama S. Spatiotemporal dynamics of turbulent coaxial jet analyzed by symbolic information-theory quantifiers and complex-network approach. Chaos 2019;29(12):123110.
[14] Epstein IR, Berenstein IB, Dolnik M, Vanag VK, Yang L, Zhabotinsky AM. Coupled and forced patterns in reaction–diffusion systems. Phil Trans R Soc A 2008;366(1864):397–408. http://dx.doi.org/10.1098/rsta.2007.2097.
[15] Castelino JK, Ratliff DJ, Rucklidge AM, Subramanian P, Topaz CM. Spatiotemporal chaos and quasipatterns in coupled reaction–diffusion systems. Physica D 2020;409:132475. http://dx.doi.org/10.1016/j.physd.2020.132475.
[16] Rubin A, Riznichenko G. Spatiotemporal self-organization of biological systems. In: Mathematical biophysics. Springer; 2014, p. 35–54.
[17] Lapine M, Shadrivov IV, Kivshar YS. Colloquium: Nonlinear metamaterials. Rev Modern Phys 2014;86(3):1093–123. http://dx.doi.org/10.1103/RevModPhys.86.1093.
[18] Shelby RA, Smith DR, Schultz S. Experimental verification of a negative index of refraction. Science 2001;292(5514):77–9. http://dx.doi.org/10.1126/science.1058847.
[19] Shelby RA, Smith DR, Nemat-Nasser SC, Schultz S. Microwave transmission through a two-dimensional, isotropic, left-handed metamaterial. Appl Phys Lett 2001;78(4):489–91. http://dx.doi.org/10.1063/1.1343489.
[20] Fang X, Wen J, Yin J, Yu D, Xiao Y. Broadband and tunable one-dimensional strongly nonlinear acoustic metamaterials: Theoretical study. Phys Rev E 2016;94(5):1–10. http://dx.doi.org/10.1103/PhysRevE.94.052206.
[21] Kaneko K. Pattern dynamics in spatiotemporal chaos. Physica D 1989;34(1–2):1–41. http://dx.doi.org/10.1016/0167-2789(89)90227-3.
[22] Wang M, Wang X, Wang C, Xia Z, Zhao H, Gao S, Zhou S, Yao N. Spatiotemporal chaos in cross coupled map lattice with dynamic coupling coefficient and its application in bit-level color image encryption. Chaos Solitons Fractals 2020;139:110028. http://dx.doi.org/10.1016/j.chaos.2020.110028.
[23] Savi MA. Effects of randomness on chaos and order of coupled logistic maps. Phys Lett A 2007;364(5):389–95. http://dx.doi.org/10.1016/j.physleta.2006.11.095.
[24] Guedes AV, Savi MA. Spatiotemporal chaos in coupled logistic maps. Phys Scr 2010;81(4). http://dx.doi.org/10.1088/0031-8949/81/04/045007.
[25] Savi MA, Pacheco PMCL. Chaos in a two-degree of freedom duffing oscillator. J. Braz Soc Mech Sci 2002;24(2):115–21. http://dx.doi.org/10.1590/S0100-73862002000200006.
[26] Kovacic I, Brennan MJ. The Duffing equation: nonlinear oscillators and their behaviour. John Wiley & Sons; 2011.
[27] Umberger DK, Grebogi C, Ott E, Afeyan B. Spatiotemporal dynamics in a dispersively coupled chain of nonlinear oscillators. Phys Rev A 1989;39(9):4835–42. http://dx.doi.org/10.1103/PhysRevA.39.4835.
[28] Chatterjee AK, Kundu A, Kulkarni M. Spatiotemporal spread of perturbations in a driven dissipative duffing chain: An out-of-time-ordered correlator approach. Phys Rev E 2020;102(5):052103. http://dx.doi.org/10.1103/PhysRevE.102.052103.

[29] Musielak DE, Musielak ZE, Benner JW. Chaos and routes to chaos in coupled Duffing oscillators with multiple degrees of freedom. Chaos Solitons Fractals 2005;24(4):907–22. http://dx.doi.org/10.1016/j.chaos.2004.09.119.
[30] Romeo F, Rega G. Wave propagation properties in oscillatory chains with cubic nonlinearities via nonlinear map approach. Chaos Solitons Fractals 2006;27(3):606–17. http://dx.doi.org/10.1016/j.chaos.2005.04.087.
[31] Hilborn RC, et al. Chaos and nonlinear dynamics: an introduction for scientists and engineers. Oxford University Press on Demand; 2000.
[32] Savi MA. Dinâmica não-linear e caos. Editora E-papers; 2006.
[33] Pikovsky A, Politi A. Lyapunov exponents: a tool to explore complex dynamics. Cambridge University Press; 2016.
[34] Shibata H. Lyapunov exponent of partial differential equation. Physica A 1999;264(1–2):226–33. http://dx.doi.org/10.1016/S0378-4371(98)00445-2.
[35] Clerc M, Coulibaly S, Ferré M, Rojas R. Chimera states in a Duffing oscillators chain coupled to nearest neighbors. Chaos 2018;28(8):083126.
[36] Ruelle D. Thermodynamic formalism: the mathematical structure of equilibrium statistical mechanics. Cambridge University Press; 2004.
[37] Grassberger P. Information content and predictability of lumped and distributed dynamical systems. Phys Scr 1989;40(3):346.
[38] Cross MC, Hohenberg PC. Pattern formation outside of equilibrium. Rev Modern Phys 1993;65(3):851.
[39] Moon F, Holmes PJ. A magnetoelastic strange attractor. J Sound Vib 1979;65(2):275–96. http://dx.doi.org/10.1016/0022-460X(79)90520-0.
[40] Costa LG, Monteiro LLS, Pacheco PMCL, Savi MA. A parametric analysis of the nonlinear dynamics of bistable vibration-based piezoelectric energy harvesters. J Intell Mater Syst Struct 2021;32(7):699–723. http://dx.doi.org/10.1177/1045389X20963188.
[41] Fang X, Wen J, Bonello B, Yin J, Yu D. Wave propagation in one-dimensional nonlinear acoustic metamaterials. New J Phys 2017;19(5):21–3. http://dx.doi.org/10.1088/1367-2630/aa6d49.
[42] Coulais C, Sounas D, Alù A. Static non-reciprocity in mechanical metamaterials. Nature 2017;542(7642):461–4. http://dx.doi.org/10.1038/nature21044.
[43] Brandenbourger M, Locsin X, Lerner E, Coulais C. Non-reciprocal robotic metamaterials. Nature Commun 2019;10(1):1–8. http://dx.doi.org/10.1038/s41467-019-12599-3.
[44] Giacomelli G, Hegger R, Politi A, Vassalli M. Convective Lyapunov exponents and propagation of correlations. Phys Rev Lett 2000;85(17):3616–9. http://dx.doi.org/10.1103/PhysRevLett.85.3616.
[45] Pikovsky AS. Local Lyapunov exponents for spatiotemporal chaos. Chaos 1993;3(2):225–32. http://dx.doi.org/10.1063/1.165987.
[46] Pazó D, López JM, Politi A. Diverging fluctuations of the Lyapunov exponents. Phys Rev Lett 2016;117(3):034101.
[47] Wolf A, Swift JB, Swinney HL, Vastano JA. Determining Lyapunov exponents from a time series. Physica D 1985;16(3):285–317. http://dx.doi.org/10.1016/0167-2789(85)90011-9.
[48] Rosenstein MT, Collins JJ, De Luca CJ. A practical method for calculating largest Lyapunov exponents from small data sets. Physica D 1993;65(1–2):117–34.
[49] Livi R, Politi A, Ruffo S. Distribution of characteristic exponents in the thermodynamic limit. J Phys A: Math Gen 1986;19(11):2033.
[50] Isaacson E, Keller HB. Analysis of numerical methods. Courier Corporation; 2012.